Waste Management 166 (2023) 141–151

Contents lists available at ScienceDirect

Waste Management

journal homepage: www.elsevier.com/locate/wasman

Research Paper

Carbon nanotubes production from real-world waste plastics and the pyrolysis behaviour

Yuan Zhu [a], Jie Miao [b], Yingrui Zhang [a], Chunchun Li [a], Yuanyuan Wang [a], Yi Cheng [c], Mingce Long [d,*], Jiawei Wang [c,*], Chunfei Wu [a,*]

[a] School of Chemistry and Chemical Engineering, Queen's University Belfast, Belfast BT7 1NN, United Kingdom
[b] School of Environmental Science and Engineering, Nanjing Tech University, Nanjing 211816, China
[c] Bioenergy Research Group, EBRI, Aston University, Birmingham B4 7ET, United Kingdom
[d] School of Environmental Science and Engineering, Key Laboratory of Thin Film and Microfabrication Technology (Ministry of Education), Shanghai Jiao Tong University, 800 Dongchuan Road, Shanghai 200240, China

ARTICLE INFO

Keywords:
Waste plastics
Pyrolysis behaviour
Carbon nanotubes
Product characteristics

ABSTRACT

The investigation of the pyrolysis behaviour of real-world waste plastics (RWWP) and using them as the feedstock to produce carbon nanotubes (CNTs) could serve as an effective solution to address the global waste plastics catastrophe. This research aimed to characterize the pyrolysis behaviour of RWWP via thermogravimetric analysis (TG) and fast pyrolysis-TG/mass spectrometry (Py-TG/MS) analyses. Activation energies (131.04 kJ mol^{-1} –171.04 kJ mol^{-1}) for RWWP pyrolysis were calculated by three methods: Flynn-Wall-Ozawa (FWO) method, Kissinger-Akahira-Sunose (KAS) method, and Starink method. Py-TG/MS results indicated that the RWWP could be identified as polystyrene (RWWP-1), polyethylene (RWWP-2), polyethylene terephthalate (RWWP-3, 4), and polypropylene (RWWP-5, 6). In addition, RWWP-1, 2, 5, 6 outperform RWWP-3 and 4 as sources of carbon for producing CNTs. The results showed a high carbon yield of 32.21 wt% and a high degree of CNT purity at 93.04%.

1. Introduction

Since the beginning of the last century, plastic manufacturing has witnessed an exponential increase to meet burgeoning social demand. Plastics have an unshakable position in the marketplace, such as healthcare, building, engineering, transportation, and aerospace(Al-Salem et al., 2017; Yan, 2022). However, the dependency on plastics results in>350 Mt of plastics being produced annually and meanwhile, almost 80% of the plastics is turned into waste(Martin et al., 2021). The proliferation of plastic products and the inadequate management of their disposal have resulted in a significant increase in environmental pollution, which poses a serious threat to our planet. Moreover, in light of the heightened public apprehension regarding the worldwide outbreak of Covid-19, it is imperative to implement a cleaner and safer approach for the disposal and management of the fast growing medical plastic waste(Adyel, 2020; Igalavithana et al., 2022). Plastic wastes have a cumulatively negative impact on the ecosystem, which has been escalating into a worldwide crisis(Macleod et al., 2021). It is universally acknowledged that waste plastics have extensive detrimental effects on air(Chu et al., 2021), soil(Chae and An, 2018), and aqueous systems (Alimi et al., 2018; Galgani and Loiselle, 2021) and eventually pose a direct hazard to human health(Leslie et al., 2022).

Real-world waste plastics management is an even more severe global problem. They were discarded worldwide annually at an astonishing rate of around 300 Mt, comprising nearly>10% of municipal solid waste (MSW) each year(Lebreton and Andrady, 2019). A significant amount of research focuses on plastics with defined and specific physicochemical qualities, while limited studies have investigated genuine waste plastics with unknown compounds. Hence, it is essential to undertake the thermal degradation process in an anonymous manner and to undertake further investigations into the pyrolysis characteristic parameters. Along with assessing the pyrolysis potential of RWWP, the possible identification of the type of feedstock is also necessary to deepen the understanding of the relation between RWWP properties and the application of their pyrolysis products. Thermogravimetric analysis (TG) under different heating rates can be employed to study the pyrolysis behaviour. Besides, the activation energy values for RWWP pyrolysis can be calculated using model-free methodologies: Starink method, Flynn –

* Corresponding authors.
E-mail addresses: long_mc@sjtu.edu.cn (M. Long), j.wang23@aston.ac.uk (J. Wang), c.wu@qub.ac.uk (C. Wu).

https://doi.org/10.1016/j.wasman.2023.05.002
Received 14 February 2023; Received in revised form 11 April 2023; Accepted 1 May 2023
Available online 10 May 2023

Wall − Ozama method, and Kissinger − Akahira − Sunose method (Das and Tiwari, 2017). The activation energy values for the activation energies for different polymers were reported as Polystyrene (PS, 168–268 kJ mol^{-1}), Polyethylene (PE, 215–247 kJ mol^{-1}), Polyethylene Terephthalate (PET, 153–265 kJ mol^{-1}), and Polypropylene(PP, 179–188 kJ mol^{-}) (Patnaik et al., 2019). Furthermore, the chemical composition of the pyrolysis products can be analyzed through the utilization of pyrolysis gas chromatography in conjunction with mass spectrometry (Akoueson et al., 2021).

In the meantime, recycling has been developed as a more environmentally friendly treatment than landfill to manage RWWP. Mechanical recycling is commonly employed, but plastics recycled in this manner are generally energy and capital-intensive and downcycled into low-grade products. The disposal of waste plastics is often approached through incineration, which is preferred over mechanical recycling. However, the combustion of waste plastics results in the release of toxic gases into the environment. In comparison, pyrolysis provides a more environmentally sustainable method of waste plastic management, as compared to traditional incineration methods(Dai et al., 2022). Since the thermal process is conducted without air participating, unfavourable end products (e.g., CO_2) can be avoided to the maximum extent. Pyrolysis is also the reverse process of manufacturing plastic products from petroleum, allowing intractable waste plastics to be converted into high-value products. Additionally, this technology keeps pace with the worldwide trend toward carbon neutrality by facilitating the energy structure transition from fossil fuels to sustainable renewable sources (He et al., 2022). Among the end products (such as oil, char, and gas), CNTs, using waste plastics as carbon sources, are regarded as outstanding items via a chemical vapour deposition method (Williams, 2021; Wu et al., 2014b). Yao et al. (Yao et al., 2021) revealed that a pyrolysis-catalysis process was employed to synthesise CNTs from post-consumer mixed waste plastics, utilising Ni-Fe bimetallic catalysts supported on four distinct porous materials (Ni-Fe/MCM41, Ni-Fe/ZSM5, Ni-Fe/Beta, and Ni-Fe/NKF5). The highest catalytic activity for waste plastic pyrolysis-catalysis, based on a carbon material yield of 55.60 wt %, was exhibited by the Ni-Fe/MCM41 catalyst. A comparative investigation of the effectiveness of three different catalysts (Fe/cordierite, Ni/cordierite, and Ni-Mg/cordierite) for the catalytic pyrolysis of waste plastics revealed that the Ni-Mg/cordierite catalyst exhibited the highest filamentous carbon yield of approximately 93 wt%(Wang et al., 2020). It is reported by Cai et al. (Cai et al., 2021b) that approximately 42 wt% carbon deposit yield can be obtained through the catalytic pyrolysis process using waste plastics when the ratio of Fe/Al_2O_3 was 1:1. Besides, the economic viability of producing CNTs through the process of catalytic pyrolysis utilizing waste plastics has been demonstrated(Cai et al., 2021b). Meanwhile, as an alternative to commercial CNTs, CNTs produced from waste plastics have demonstrated extraordinary competitiveness in many research fields, such as solid oxide fuel cells(Liu et al., 2022), pollutant adsorption(Yao et al., 2022), electrocatalysts(Cai et al., 2020), phase change material(Wang et al., 2022).

It is noted that the combined investigation on the pyrolysis behaviour of genuine RWWP followed by producing high-value CNTs is very limited in the open literature. The goal of this work is to advance the innovation in synthesizing high-value CNTs from RWWP by researching the pyrolysis characteristic parameters and product composition. The bridge was built to enhance the understanding between waste plastics and end products. In addition, the feasibility of CNTs production using different RWWP samples was inspected by employing a range of technical methods, including XRD, SEM, TEM, Raman, and BET.

2. Experimental section

2.1. Materials and pyrolysis procedure

The plastic raw material utilized in this work was sourced from ReGen Ltd, UK. The waste plastics were cut into small squares (~5 mm). According to their colour and density, the real-world waste plastics were roughly classified into six categories, which were assigned as RWWP-n (n = 1–6), respectively. Table S1 presents the data of the proximate and ultimate analysis of the RWWP samples.

The thermal degradation of the RWWP samples was studied using TGA 2950 thermogravimetric analyzer. In each trial, 5–10 mg of RWWP sample was used and subjected to heating from room temperature to 600 °C under N_2 at 10, 20, and 30 °C min^{-1}, respectively. The pyrolysis and combustion kinetics of plastics were predominantly characterized by the first-order Arrhenius law. The Coats-Redfern integral method was employed to ascertain the activation energy for non-isothermal degradation of RWWP samples in this work. Consequently, the rate equation for kinetics analysis may be formulated as:

$$\frac{d(\alpha)}{d(t)} = f(\alpha)k(T) \tag{1}$$

$$\alpha = \frac{m_0 - m_t}{m_0 - m_f} \tag{2}$$

where α represents reaction conversion degree, and m_0, m_t, m_f is weight at the initial stage, weight at actual time, weight at the final stage, respectively; T refers to reaction temperature, and t is reaction time; f(α) is the kinetic model which represents the reaction mechanism function; k(T) is the reaction rate constant. According to Arrhenius law,

$$k(T) = Aexp(-\frac{E}{RT}) \tag{3}$$

where A works as the pre-exponential factor; R represents the gas constant; E describes the activation energy, kJ mol^{-1}.

Coupling heating rate β = d(T))/d(t) and Eq. (1) into Eq. (3) can obtain:

$$\frac{d(\alpha)}{f(\alpha)} = \frac{A}{\beta}exp(-\frac{E}{RT})d(T) \tag{4}$$

Eq. (4) can be integrated when α = 0 and T = T_0, and then the kinetics of the pyrolysis reaction were represented as Eq. (5)(Ding et al., 2021; Qu et al., 2019):

$$G(\alpha) = \int_0^{\alpha} \frac{d(\alpha)}{f(\alpha)} = \frac{A}{\beta}\int_{T_0}^{T} exp(\frac{-E}{RT})dT \approx \frac{A}{\beta}\int_0^{T} exp(\frac{-E}{RT})dT \tag{5}$$

Consequently, activation energy (E) can be calculated by FWO, KAS, and Starink methods, respectively, which are defined as Eq. (2–4):

$$\ln\beta = \ln\frac{AE}{RG(\alpha)} - 5.331 - 1.052\frac{E}{RT} \tag{6}$$

$$\ln\frac{\beta}{T^2} = \ln\frac{AR}{EG(\alpha)} - \frac{E}{RT} \tag{7}$$

$$\ln\frac{\beta}{T^{1.92}} = \ln\frac{AE}{RG(\alpha)} - 1.0008\frac{E}{RT} \tag{8}$$

where α, β refers to the reaction conversion degree and heating rate; $G(\alpha)$ is the kinetic model; E describes the activation energy, kJ mol^{-1}; A works as the pre-exponential factor; R represent the gas constant.

Furthermore, the composition of the pyrolysis products was characterized using Py-GC/MS. This analytical setup consisted of a Shimadzu GCMS-QP2010 SE and a Multi-Shot Pyrolyzer EGA/PY-3030 D. During each test, the samples were heated at 500 °C with 2 mg of injection volume. The resulting volatiles were analyzed through a GC column (Rtx-5, 30 m × 0.25 mm × 0.25 μm) and an EI (Electron Ionization) mass spectrometer. The sample was injected at a split injection mode with a 50:1 split ratio using helium (99.99%) as the carrier gas (54.1 mL min^{-1}). The MS scan was performed at 45–300 m/z, with a scanning interval of 0.3 s and a speed of 1666. The peaks were identified using the NIST mass spectrometry library and literature.

2.2. Pyrolysis–catalysis catalysts and reactor system

The Fe-based catalyst was obtained by using a wet impregnation method. The necessary materials, $Fe(NO_3)_3{\cdot}9H_2O$, Al_2O_3 and ethanol, were purchased from Sigma-Aldrich (UK). $Fe(NO_3)_3{\cdot}9H_2O$ was dissolved in ethanol, then Al_2O_3 was added and stirred. The mixed precursor was put in a heating oil bath and then in an oven to form a slurry. The final product was dried overnight at 100 °C. The prepared catalyst precursors were transformed into a muffle furnace and calcinated for 3 h at 800 °C. Finally, the $Fe@Al_2O_3$ catalyst was collected after the muffle furnace cooled down to room temperature.

As displayed in Fig. S1, the CNTs production experiments using RWWP were employed in a two-stage reactor. The system with two separate electrical furnaces provided corresponding pyrolysis and catalysis zones for heating the quartz tube reactor. Each furnace was independently monitored and controlled. The experiments in this work were conducted using N_2 as an inert gas (100 mL min^{-1}). 1 g of RWWP was placed in a cylindrical quartz container in the upper reactor, while 0.25 g of $Fe@Al_2O_3$ was evenly placed on quartz wool in the center of the lower tube reactor. The lower reactor was firstly heated to 800 °C at a rate of 20 °C min^{-1}. The target temperature of upper furnace was reached, and the RWWP sample in the upper reactor was then heated to 500 °C at a heating rate of 10 °C min^{-1} and kept isothermal for 10 min. The resulting black powder was collected. The carbon products obtained from different RWWP were assigned as PRWWP-n (n = 1–6). Carbon yield can be calculated using Eq. (4):

$$Carbon\ yield = \frac{Mass\ of\ reacted\ catalyst - mass\ of\ fresh\ catalyst}{Mass\ of\ plastic\ used} \times 100\%(wt.\%) \quad (9)$$

2.3. Product characterization

The products were characterized by several different techniques. Temperature-programmed oxidation (TPO) for the products was conducted using the TGA 2950 thermogravimetric analyzer under the air atmosphere. XRD was employed on a PANalytical Empyrean series 2 diffractometer with Cu Kα X-ray source. The surface morphology and diameter of the products were analyzed using SEM and TEM, specifically with a FEI Quanta FEG Oxford Ex-ACT scanning electron microscope and a TECNA1 G2F20 transmission electron microscopy. The extent of graphitization of the carbon products was analyzed by a Raman spectrometer (WITec Alpha 300R Confocal Raman Microscope: laser wavelength = 532 nm, spectra = 1000–3500 cm^{-1}). Using a nitrogen adsorption measurement system (Micromeritics Tristar 3020) at −196 °C, the pore size distribution (D_{pore}, nm), total pore volume (V, cm^3g^{-1}), specific surface area (S_{BET}, m^2g^{-1}) of the products were analyzed by the Brunauer–Emmett–Teller (BET) method.

3. Results and discussion

3.1. Characterization of RWWP

Fig. 1 illustrates the thermogravimetric (TG) and differential thermogravimetric (DTG) behavior of RWWP in a nitrogen atmosphere at 10, 20, and 30 °C min^{-1}, respectively. The results demonstrate that the thermogravimetric and differential thermogravimetric curves move towards lower temperatures as the heating rate increases, which implies that the rate of weight loss in the samples becomes more rapid. This phenomenon can be attributed to two factors: thermal hysteresis and limitations in heat transfer(Ding et al., 2021). The results in Fig. 1 further reveal that the maximum weight loss rate for all RWWP samples ascends as heating rate increased from 10 to 30 °C min^{-1}. Additionally, the pyrolysis process of all RWWP samples in the work is characterized by a single stage, as evidenced by the presence of only one distinct peak in each DTG curve. It is further implied that the main component of each RWWP in this work was single. On the other hand, an inspection of the end of the TG curves reveals that the weight ratio of solid residue for different RWWP samples was different. For example, the residue mass of RWWP-3,4 was significantly larger than that of RWWP-1,2,5,6, which indicated that RWWP-3,4 contained less volatile content. In other words, the samples of RWWP-1,2,5,6 were easier to generate hydrocarbon gases rather than ash residues. The pyrolysis process was more advantageous when the amount of volatile matter was higher to generate higher gas production and caloric value (Ding et al., 2021).

Pyrolysis characteristic parameters for different RWWP samples are displayed in Table 1. The data indicate that the pyrolysis process of all RWWP samples occurred between 330 and 560 °C. The concentrated pyrolysis temperature range indicated that the pyrolysis reaction was fast, and the RWWP samples in this work exhibited high pyrolysis potential. The pyrolysis temperature zone is close to the findings in Xu et al.'s work, and they reported that the pyrolysis interval was

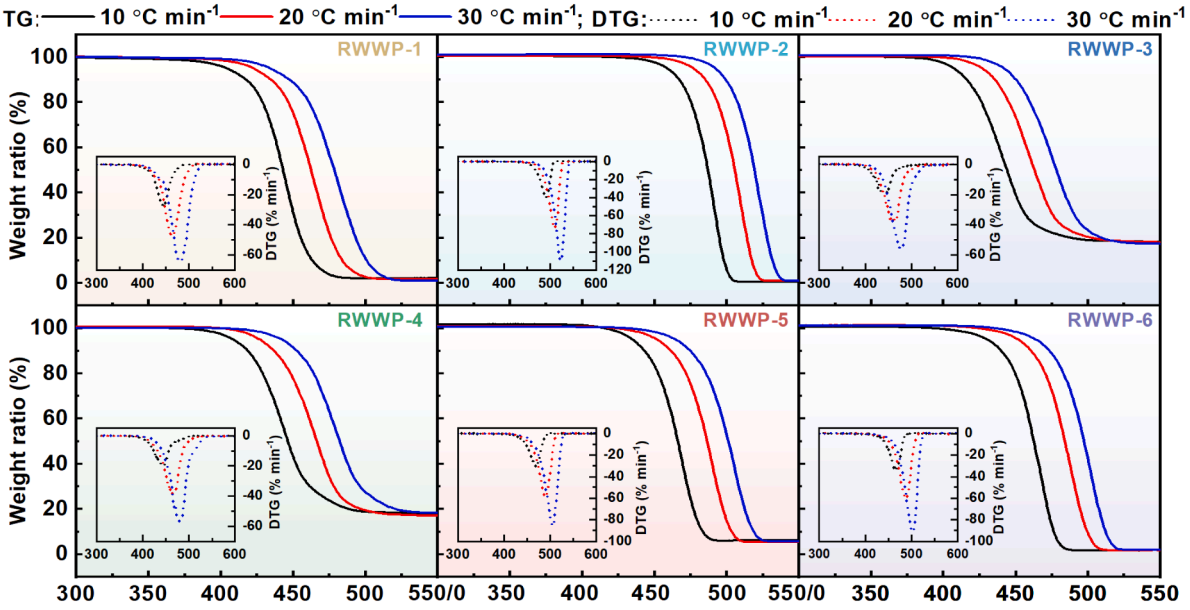

Fig. 1. TG and DTG patterns of RWWP samples with different heating rate: 10, 20, and 30 °C min^{-1}.

Table 1
Pyrolysis characteristic parameters for RWWP-n (n = 1–6) samples.

Plastic Samples	Heating rate (°C min^{-1})	T_s[a] (°C)	T_f[b] (°C)	T_{max}[c] (°C)	DTG_{max}[d] (wt.% min^{-1})	DTG_{mean}[e] (wt.% min^{-1})	$\Delta T_{1/2}$[f] (°C)	D[g](x10^{-7}) (wt.%^{2} min^2 °C^3)
RWWP-1	10	364.92	494.61	444.93	−27.36	−7.44	30.41	4.10
	20	382.68	516.68	463.04	−47.49	−14.53	35.26	10.99
	30	395.52	532.71	481.23	−64.61	−21.34	40.49	17.81
RWWP-2	10	411.00	510.57	490.43	−40.01	−9.98	22.28	8.84
	20	417.41	528.13	508.98	−74.10	−17.85	22.60	27.41
	30	431.66	546.99	523.27	−109.68	−25.89	23.76	52.64
RWWP-3	10	365.84	515.09	444.44	−19.28	−5.46	35.97	1.52
	20	372.30	534.36	452.56	−37.55	−10.06	37.19	5.08
	30	385.94	549.57	478.00	−56.22	−15.36	39.07	10.10
RWWP-4	10	331.38	514.70	444.74	−19.72	−4.45	33.00	1.54
	20	349.98	530.98	462.67	−38.76	−9.23	35.64	5.29
	30	371.09	551.44	481.77	−56.82	−13.72	33.77	11.01
RWWP-5	10	379.62	493.52	468.72	−30.21	−8.35	27.06	5.05
	20	394.52	516.19	489.72	−58.82	−15.61	27.84	16.45
	30	414.07	533.23	505.13	−86.24	−23.86	28.48	33.30
RWWP-6	10	377.74	490.23	467.99	−33.37	−8.77	26.35	6.26
	20	390.40	516.19	488.77	−60.43	−15.77	26.99	18.43
	30	407.06	531.42	502.78	−91.62	−24.18	29.38	36.70

[a] T_s, the temperature of the onset of thermal decomposition.
[b] T_f, the final decomposition temperature.
[c] T_{max}, the temperature related to the largest weight loss rate.
[d] DTG_{max}, the highest weight loss rate.
[e] DTG_{mean}, the average weight loss rate.
[f] $\Delta T_{1/2}$, the half-peak width of the DTG curve.
[g] D, the characteristic index for pyrolysis.

391–551 °C for PP and 440–572 °C for PE, respectively(Xu et al., 2018). To enhance the characterization of the pyrolysis behavior, a comprehensive pyrolysis characteristic index (referred to as index D) was introduced (Fang et al., 2015; Peng et al., 2015). The degree of the thermal degradation process difficulty could be represented by index D, which can be expressed as Eq. (5):

$$D = \frac{(dm/dt)_{mean} \times (dm/dt)_{max} \times m_{\infty}}{T_s T_{max} \Delta T_{1/2}} \tag{10}$$

Where $(dm/dt)_{mean}$ and $(dm/dt)_{max}$ correspond to the mean and largest weight loss rate. m_{∞} represents the pyrolysis mass loss. T_s and T_{max} are used to denote the temperature of the onset of thermal decomposition process and the temperature related to the maximum weight loss rate, respectively. $\Delta T_{1/2}$ is defined as the half-peak width for the DTG curves.

The larger value of $(dm/dt)_{mean}$, the larger value of $(dm/dt)_{max}$ and the smaller value of T_s represents an easier and more vibrant release of volatiles. In addition, the smaller value of T_{max} and $\Delta T_{1/2}$ demonstrates that the weight loss peak occurred earlier. The bigger index D represents the more vigorous decomposition of plastic, which is related to the easier and more dramatic pyrolytic reaction. As displayed in Table 1, the index D of RWWP-1,2,5,6 was larger than that of the RWWP-3,4, especially when the heating rate was increasing. It is implied that the carbon formation process was easier to be produced during the thermal degradation process of RWWP-1,2,5,6(Jung et al., 2010). Furthermore, the values of $(dm/dt)_{max}$ and index D for RWWP samples ascended with rising heating rate, suggesting that pyrolysis efficiency may be enhanced by pyrolysing plastics at a high heating rate. When municipal solid waste was thermal degraded at a high heating rate, rapid biomass fragmentation and increased volatile products could be obtained(Qiao et al., 2018). In addition, the values of DTG_{max} and D_i (the devolatilization index) increased with a higher heating rate for processing food waste, demonstrating that the pyrolysis process might be improved(Ming et al., 2020).

As a result of the stronger interaction between the sample molecules, the higher E value showed that more energy was needed to start the reactions(Zou et al., 2019). In Table S2-S4, three methods, namely FWO, KAS, and Starink methods, were applied at different conversion levels, with a step of 0.1, to accurately determine the activation energy values and their correlation coefficient (R^2) for the thermal degradation of the RWWP samples. An inspection of the data in Table S2-S4 reveals that the E values obtained by different methods were very close, and the R^2 values were all in the range of 90.67–99.99%. The mean E values for RWWP samples were found to lie within the range from 131.04 kJ mol^{-1} to 171.04 kJ mol^{-1}. Furthermore, the difference among the E values was attributed to the distinction in the component or molecular structure of plastic samples(Zhang et al., 2022). Recent studies also reported the activation energy for other types of municipal solid wastes. For example, the activation energy for paper sludge, pine sawdust, and rice husk was 133.98 kJ mol^{-1}, 108.18 kJ mol^{-1}, 185.7 kJ mol^{-1}, respectively(Fang et al., 2015; Gao et al., 2013; Loy et al., 2018). Therefore, different E values are obtained for the RWWP samples and the above-studied municipal solid wastes. This can be attributed to the fact that the decomposition reaction of different municipal solid wastes is needed to break different levels of energy barriers. In other words, a higher E value indicated that it was more challenging for the substance to be degraded (Chen et al., 2015). Moreover, since each reaction has a unique activation energy at various conversions, the activation energy for different RWWP samples pyrolysis significantly changed with conversion, which was displayed in Table S2-S4. It was noteworthy to observe that, for the pyrolysis of various RWWP samples, the activation energy value was small for the initial step of conversion at 0.1, except for RWWP-1. This phenomenon has been attributed to the presence of increased reaction rate or thermally labile bonds in the polymer chains(Das and Tiwari, 2017). These findings are anticipated to contribute to comprehending the intricacies of the pyrolysis methodology as applied to waste plastics in real-world scenarios.

Total ion chromatograms of RWWP-n (n = 1–6) are shown in Fig. S2 and the identification of the peaks is presented in Table S5-S10. The pyrolysis products of different waste plastics are various, as the cracking process is very diverse. Styrene, styrene dimer, and styrene trimer were reported to be the principal products of PS pyrolysis, while PE pyrolysis produced C_4-C_{35} hydrocarbon(Sophonrat et al., 2017; Zhang et al., 2022). Besides, a similar composition was found in PP pyrolysis products when it was compared to PE pyrolysis products. The differing point is that alkanes from PP pyrolysis products usually contained a branched

chain, as the methyl groups existed in the PP molecular(Das and Tiwari, 2018). In terms of PET, low hydrocarbon content was produced, and gases produced from PET contained CO_2 since oxygen is a component of its molecular structure $(C_{10}H_8O_4)_n$(Honus et al., 2018). In this work, styrene ranked at the top (51.59%) of RWWP-1 pyrolysis products, followed by cyclohexane (32.90%) and toluene (2.98%). For RWWP-2 pyrolysis products, compounds with a benzene ring can barely be observed. The main products included heneicosane (16.45%), n-tetracosanol-1 (10.16%), 1,19-eicosadiene (9.98%), etc. In terms of RWWP-3,4, their main products are compounds with oxygen-containing functional groups, in which 4-acetylbenzoic acid, benzoic acid, methyl tetratriacontyl ether, accounted for the top three portions. For RWWP-5, 6, the pyrolysis products were cyclohexane, 1-heptene, 11-methyldodecanol, etc. To be more specific, the main products (top three compounds) from RWWP-n (n = 1–6) pyrolysis are displayed in Table 2. Overall, the evidence from Py-GC/MS analysis suggests that the possible definition for RWWP-1 was PS, RWWP-2 was PE, RWWP-3,4 was PET and RWWP-5,6 was PP. Thus, based on their varying chemical compositions and thermal decomposition products, RWWP-1, 2, 5, 6 are deemed more suitable as a carbon source for producing carbon nanotubes compared to RWWP-3, 4.

3.2. Characterization of fresh catalyst

The physical property of the prepared fresh Fe@Al_2O_3 catalyst was characterized by several technologies. The XRD of the fresh Fe@Al_2O_3 catalyst identified the presence of Fe_2O_3, and Al_2O_3, as shown in Fig. 3 (a). The crystallite dimension of Fe_2O_3 has been calculated to be 31.30 nm through the utilization of the Scherrer equation. It is suggested active Fe species were well dispersed on the surface of Al_2O_3. The Fig. 2 (b) displays the results of N_2 absorption and desorption(BET) for Fe@Al_2O_3 catalyst. Fe@Al_2O_3 displays Type II isotherms behavior and H3 hysteresis looping pattern. Within elevated relative pressures (around 0.5–1.0), the latter resulted in the development of slit-like pores, which enabled the arrangement of plate-like particles in a stacked configuration, which could be commonly shown in mesoporous materials(Cao et al., 2021). The specific surface area, pore volume, and average pore diameter of the fresh Fe@Al_2O_3 catalyst were 1.05 $m^2\ g^{-1}$, 0.01 $cm^3\ g^{-1}$, and 77.63 nm, respectively. Besides, Fig. 2(c, d) illustrates the morphology of the fresh Fe@Al_2O_3. Fig. 2(c) depicts the low magnification microscopy of the catalyst exhibiting a crystalline structure, while Fig. 2(d), which displays high magnification microscopy, reveals the presence of a substantial number of small catalyst particles that were aggregated on the surface of the Al_2O_3 substrate.

3.3. Characterization of carbon products from pyrolysis-catalysis of RWWP

Fig. 3 shows XRD patterns, Raman spectra, N_2 absorption–desorption patterns, and pore size distribution patterns of the carbon products obtained from RWWP samples. As shown in Fig. 3(a), the crystalline phases of all the carbon deposition can be indexed into three categories, which are Al_2O_3, C, and Fe, respectively. The peaks corresponding to Al_2O_3 in the fresh catalyst as depicted in Fig. 2(a) were found to be comparable to those of pure Al_2O_3, indicating a high degree of thermal stability for Al_2O_3. Besides, it is worth noting that new peaks appeared at around $2\theta = 26.4^\circ$ when RWWP-1,2,5,6 was used as feedstock. The peak, associated with the (0 0 2) lattice plane, could be referred to as graphite, which was reported in previously published works (Deck and Vecchio, 2006; Weizhong et al., 2004). Conversely, when the XRD result of Fe@Al_2O_3, as presented in Fig. 2(a), is compared to that of the new catalyst, newly observed peaks at around 44.7°, which are indicative of iron, are discernible in Fig. 3. The appearance of metallic iron can be understood by the reduction of hematite at heating: hematite can be first transformed into magnetite at about 400 °C; then, with the consumption of hydrogen, magnetite can be further transformed into the unstable mineral wustite, and eventually into metallic iron(Yao et al., 2018a). The XRD patterns of all the products display peaks that correspond to metallic Fe. Specifically, the peak intensity of Fe in PRWWP-3,4 was much stronger than that in PRWWP-1,2,5,6. Additionally, no distinct graphite peak appears in XRD patterns of PRWWP-3,4. Therefore, it reveals that Fe_2O_3 in the catalyst was reduced to Fe in all experiments, but carbon deposition could only be observed using the RWWP-1,2,5,6 samples during the catalytic pyrolysis reaction. In addition, the XRD results can be utilized to calculate size of the carbon products (D_C) and Fe particles (D_{Fe}) through the application of the Scherrer equation, while the interlayer spacing for the carbon products (d_{002}) can be determined by utilizing Bragg's equation(Major et al., 2018). In Table S11, the crystallite size of PRWWP-1,2,5,6 is 5.32 nm, 7.30 nm, 7.26 nm, 7.06 nm, respectively. In terms of the Fe crystallite size, PRWWP-3 (38.10 nm) and PRWWP-3 (33.45 nm) are much larger than that of PRWWP-1,2,5,6 at 19.76 nm, 17.16 nm, 16.18 nm, 18.88 nm, respectively. It implies that catalyst particles without carbon deposition are more likely to be aggregated in larger sizes. Moreover, the number of carbon layers (N) and the degree of graphitization (g^d) can be estimated through analysis of the interlayer spacing(Maldonado-Hodar et al., 2000). An analysis of d_{002} for the carbon products suggested a slight difference from the theoretical value (0.335 nm), a phenomenon that can be attributed to the occurrence of defects during the CNTs synthesis procedure(Xia et al., 2019). The graphitization degree of the obtained carbon deposits is also presented in Table S11 for comparison purposes, with an ascending tendency in the order of PRWWP-2 > PRWWP-6 > PRWWP-5 > PRWWP-1. Furthermore, the number of carbon layers (ranging from 15 to 22) of PRWWP-1,2,5,6, indicates that the produced graphitized carbon products (CNTs in this work) might be multiwall carbon nanotubes.

The Raman spectra of the products obtained from different RWWP are depicted in Fig. 3(b). The spectra exhibit three distinctive peaks, including (1) the D peak located at approximately 1346 cm^{-1}, which is associated with amorphous or sp^3 disordered carbon structures, (2) the G peak situated at approximately 1575 cm^{-1}, which pertains to the highly ordered graphene layers found in CNTs, and (3) the G' peak at around 2680 cm^{-1}, which arises from vibrational modes characterized by the breathing of six carbons in the hexagonal lattice of graphene (Jorio and Saito, 2021). The I_D/I_G ratio measures the degree of defects and the $I_{G'}/I_G$ ratio assesses the purity of the CNTs in the products. It is

Table 2
Main products (top three compounds) from RWWP-n (n = 1–6) pyrolysis.

	Compound names	Relative content (%)		Compound names	Relative content (%)
RWWP-1	Styrene	51.59	RWWP-2	Heneicosane	16.45
	Cyclohexane, 1,3,5-triphenyl-	33.29		n-Tetracosanol-1	10.16
	Toluene	2.98		1,19-Eicosadiene	9.98
RWWP-3	4-Acetylbenzoic acid	16.09	RWWP-4	Benzoic acid	22.87
	Benzoic acid	12.15		4-Acetylbenzoic acid	19.89
	Methyl tetratriacontyl ether	11.03		Methyl tetratriacontyl ether	12.44
RWWP-5	Cyclohexane, 1,2,3,5-tetraisopropyl-	13.9	RWWP-6	Cyclohexane, 1,2,3,5-tetraisopropyl-	22.45
	1-Heptene, 5-methyl-	13.07		1-Heptene, 5-methyl-	15.03
	11-Methyldodecanol	6.25		11-Methyldodecanol	10.65

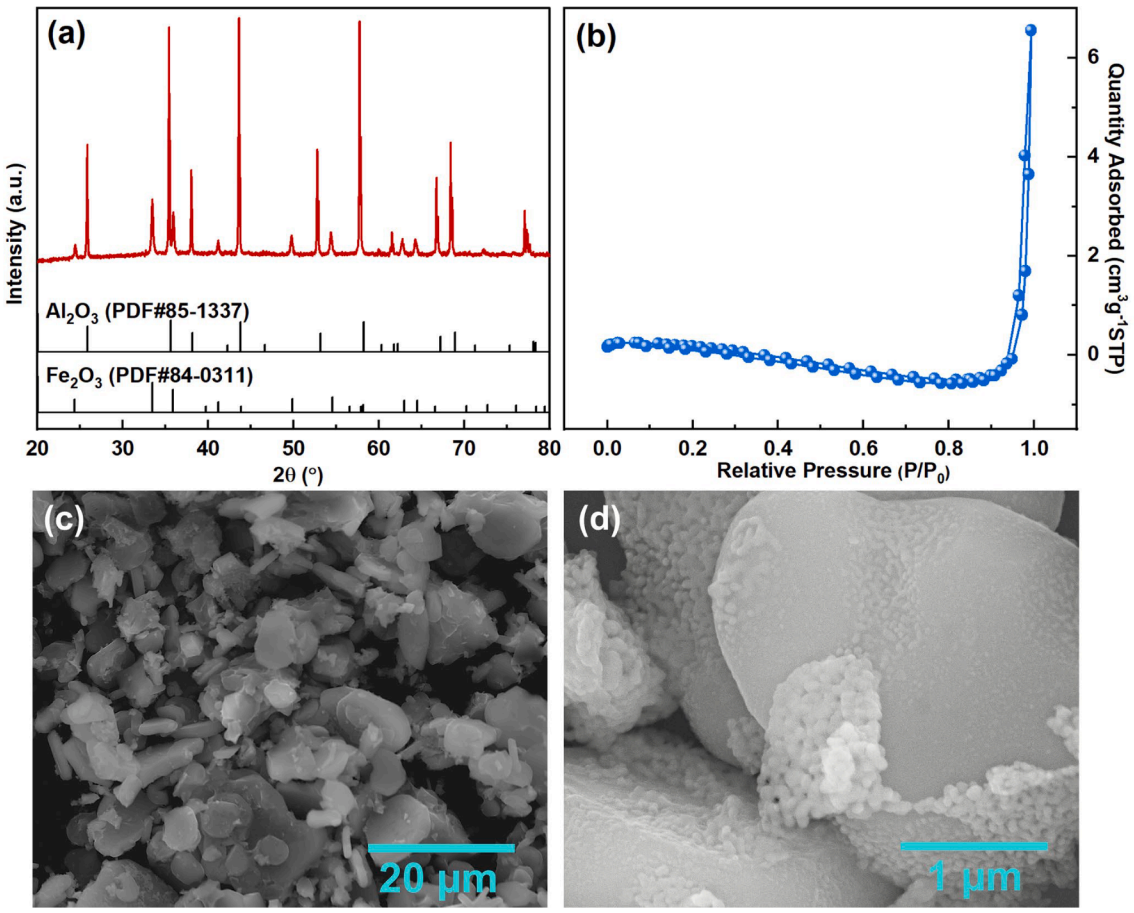

Fig. 2. The different characteristics of fresh Fe@Al_2O_3 catalyst: (a) XRD pattern, (b) N_2 absorption and desorption curve, (c, d) SEM images.

noteworthy that the broad bands exist in the pattern of PRWWP-3,4, with no distinct peak at 1346–2680 cm^{-1}, indicating limited amounts of the carbon structure. Based on the Py-TG/MS findings, it can be concluded that RWWP-3,4 can be identified as PET, which contains oxygen in its molecular structure. As a consequence of the dominant formation of CO and CO_2 during PET pyrolysis, the catalyst cannot facilitate carbon deposit, leading to the products exhibiting the lowest degree of graphitisation and CNTs purity. In contrast to the results of PRWWP-3,4, however, the Raman spectra of PRWWP-1,2,5,6 display three individual peaks. The value of I_D/I_G for responding carbon products (PRWWP-5, PRWWP-2, PRWWP-6, PRWWP-1) follows the order of $0.87 > 0.64 > 0.58 > 0.49$. The larger ratio of I_D/I_G refers to a lower degree of graphitization, and therefore the PRWWP-1 reached the lowest graphitization degree. Besides, the $I_{G'}/I_G$ ratio for PRWWP-2 exhibited the largest value, indicating the highest purity of CNTs produced. The CNTs purity can be present in the following order: PRWWP-2 > PRWWP-6 > PRWWP-5 > PRWWP-1. This is also consistent with the results of graphitization degree (g^d) in the XRD analysis. RWWP-1, 2, 5, 6 (identified as PS, PE, PP, PP, respectively) generate non-oxygenated hydrocarbons as the primary pyrolysis products, which are suitable as carbon sources for CNT synthesis. PE/PP (RWWP-2, 5, 6) waste yields a high quantity of gaseous products, whereas PS (RWWP-1) waste yields aromatic hydrocarbons with a wide distribution of carbon numbers and a higher carbon deposition with more amorphous carbon. In contrast, PE/PP (RWWP-2, 5, 6) produce more graphitic carbon deposition, suggesting their higher suitability for the production of high-purity CNTs than PS(Cai et al., 2021a).

The nitrogen adsorption–desorption isotherms and the pore size distributions for various PRWWP are depicted in Fig. 3(c, d). A closer inspection of Fig. 3(d) reveals the pore size distribution curves for PRWWP, which were obtained using the BJH method. The most prominent pores of PRWWP-1,2,5,6 are in the mesopore region, while the most probable apertures of PRWWP-3,4 are not distinct. Furthermore, Table S12 shows that the detailed parameters on pore structure for the carbon products. The highest S_{BET} of the carbon product reaches 45.65 m^2g^{-1} using RWWP-1 as the feedstock, and the S_{BET} value of PRWWP-2,5,6 is slightly smaller, which are 40.43 m^2g^{-1}, 36.40 m^2g^{-1}, 42.31 m^2g^{-1}, respectively. In terms of the average pore diameter of PRWWP-1,2,5,6, ranging from 12.21 nm to 16.90 nm, it confirms all the products have mesoporous. It is evident that the S_{BET} and pore volume of PRWWP-3,4 were significantly lower compared to the other samples and were almost equivalent to the S_{BET} and pore volume of the fresh Fe@Al_2O_3 catalyst. The catalysts covered by numerous CNTs could achieve much higher specific surface areas, which reach the maximum at 45.65 m^2g^{-1} in PRWWP-1.

The SEM images in Fig. 4 provide further insight into the structure of the produced carbon deposits. In Fig. 4(a, c, i, k), it can be observed that filamentous carbons have densely grown around the catalyst particles. At higher magnifications, as displayed in Fig. 4(b, d, j, l), it can be seen that the length of the produced CNTs can be several micrometers long, with highly entangled morphologies. This might have been caused by the interweaving of the CNTs with each other, as the presence of ash could have poisoned the metal catalyst particles and impeded their ability to produce CNTs effectively. (Yildiz et al., 2015). Nevertheless, CNTs are barely observed in terms of the SEM images of PRWWP-3 (Fig. 4(e, f)), and limited quantities of filamentous carbons were produced in terms of PRWWP-4 (Fig. 4(g, h)). Catalyst particles in Fig. 4(e, g) were correspondingly exposed as there were not enough carbon deposits.

To obtain a further understanding of the structure about the

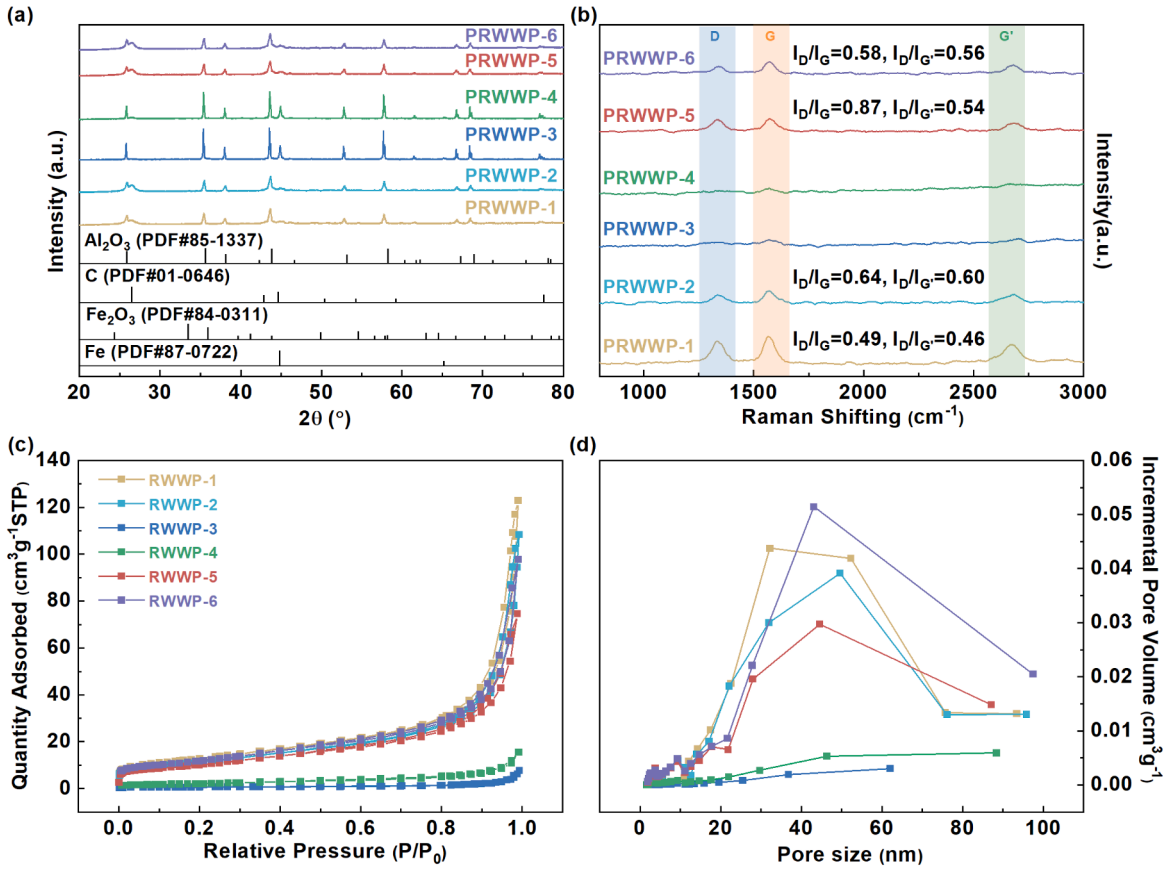

Fig. 3. The different characteristics of the products obtained from RWWP-n (n = 1–6): (a) XRD patterns, (b) Raman spectra, (c) N_2 absorption and desorption patterns (d) pore size distribution patterns.

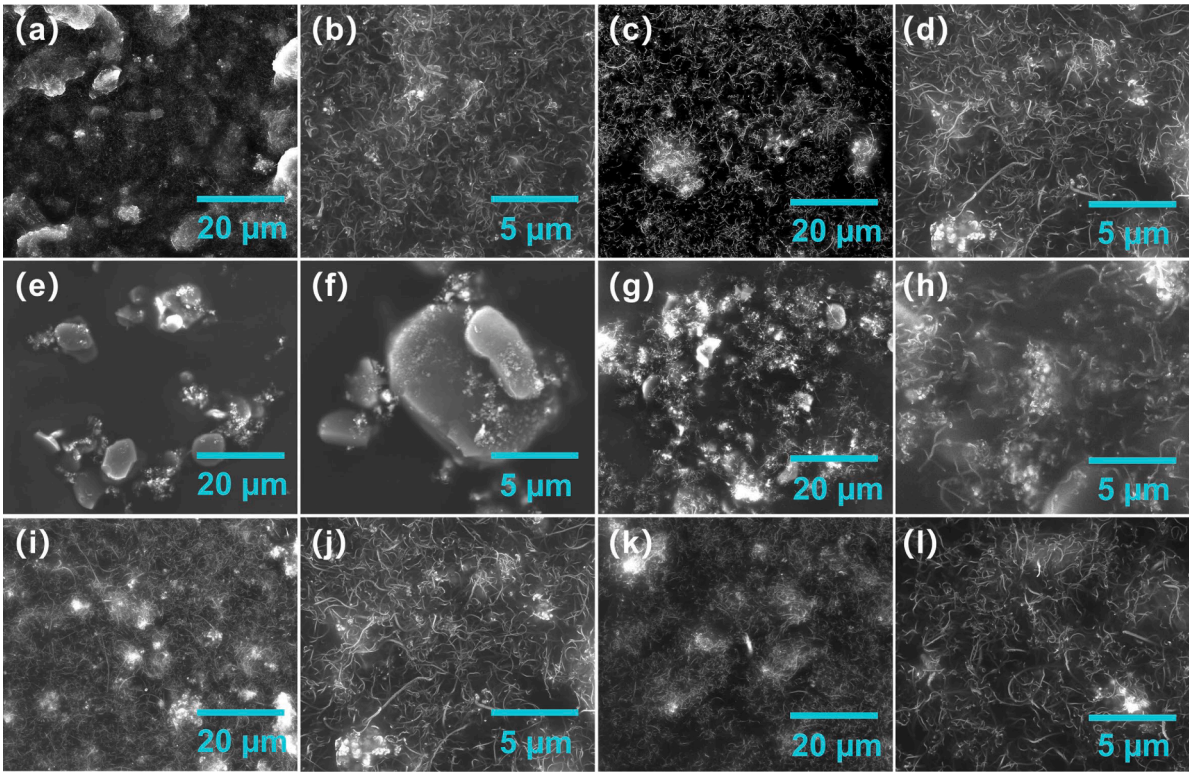

Fig. 4. SEM morphology analysis of products obtained from different RWWP: (a, b) PRWWP-1 (c, d) PRWWP-2, (e, f) PRWWP-3, (g, h) PRWWP-4 (i, j) PRWWP-5, (k, l) PRWWP-6.

produced carbon materials, TEM analysis was performed on the sample obtained from PRWWP-2. As shown in Fig. 5(a), the produced fiber-like carbons can be identified as smooth CNTs. Fig. 5(a) illustrates the diameter distribution of the fabricated CNTs, exhibiting an average outer diameter of 31.16 nm and a range of 10–60 nm, which is in close correlation with the size of the catalyst particle, as frequently reported in many literature (Chen et al., 2005; Ding et al., 2004). According to tip growth mechanism, small catalyst particles can also be observed trapped within the CNTs(Amelinckx et al., 1994). The active metal of catalysts caused the CNTs growth attributed to weak metal-support interaction, leading to the formation of metal nanoparticles at the apex or center of the CNTs(Liu et al., 2022). From Fig. 5(b), the HRTEM image confirms that the rod-like catalyst particle was encapsulated in the CNTs. The elongated shape of the catalyst particles contributes to the stress and movement during the formation of graphene layers, leading to a continuous squeeze and stretch process for the catalysts. In addition, as Golunski reported(Golunski, 2007), the Tamman temperature of metallic iron is 630 °C, which is much lower than that of the catalytic reaction in this work (800 °C). Therefore, the iron in the catalyst particles starts started to become mobile. Furthermore, the liquid-like behavior of the metal particles was attributed to their migration away from the catalyst substrate under high temperature(Kalantar-Zadeh et al., 2019). The inset TEM image in Fig. 6(b) shows a lattice fringe of 0.203 nm, indicating the (1 1 0) plane of iron, and confirming the reduction of Fe_2O_3 in the fresh catalyst to metallic Fe during the catalytic pyrolysis process.

Fig. 6 shows the degradation properties of the carbon products, which were analyzed through TPO experiments. The weight loss from the oxidation of graphite and amorphous carbons can be distinguished by their varying oxidation temperatures(Wu et al., 2014a). The weight loss occurring prior to 600 °C is attributed to the oxidation reaction of amorphous coke, while the weight loss resulting from the consumption of graphite carbon is seen at temperatures above 600 °C. An increase in the weight ratio was observed in PRWWP-3,4 at temperatures between 400 and 500 °C (Fig. 6(a)), which might be related to the oxidation process of metallic Fe(Yao et al., 2018a). In addition, it is apparent from Fig. 6(a) that the weight loss linked to PRWWP-1,2,5,6 is similar at around 50–52 wt%. In contrast, only 13 wt% of the weight loss can be observed in terms of PRWWP-4. Furthermore, no significant weight difference in PRWWP-3 before and after the TPO process. In Fig. 6(b), the oxidation peak of PRWWP-1, 2, 5, 6 was observed within a temperature range from 653 °C to 667 °C, which was significantly higher than that in the case of PRWWP-4 (No oxidation peak can be observed in PRWWP-3). It is demonstrated that the carbon deposits produced from RWWP-1,2,5,6 show higher thermal stability, linked to graphitic carbon than that obtained from RWWP-4. Together these results provide important insights into which type of RWWP could be optimal for synthesizing CNTs.

As shown in Fig. 6(c), the carbon yield was obtained using Eq. 9. The value of the carbon yield ranged from around 26–32 wt% except for PRWWP-3,4. It validated the feasibility of transforming real-world waste plastics into valuable carbon material at a considerable yield. In addition, the dominant type of carbon in the products from RWWP-1,2,5,6 was graphitic, and the proportion of graphite-type carbon followed the order of PRWWP-2 > PRWWP-6 > PRWWP-5 > PRWWP-1, which was consistent with the position sequence of the oxidation peak in Fig. 6 (b). Moreover, the results of the graphite proportion of P-RWWP agree with the order of graphitization degree (g^d) in XRD analysis (Table S11). Besides the TPO data presented in Fig. 6, which enables the characterisation of carbon deposits on the catalyst surfaces, the quantification of the ratio of carbon conversion from RWWP samples to carbon deposits on the catalysts can be evaluated by utilising the carbon content values of the RWWP samples, as provided in Table S1. The corresponding results are 35.16 wt% (RWWP-1), 34.49 wt% (RWWP-2), 32.64 wt% (RWWP-5), 35.14 wt% (RWWP-6). As for RWWP-3,4, the carbon deposition process was very limited. It can be hypothesised that the rest of carbon constituents, which were present within the RWWP samples, could have undergone volatilisation and a lesser extent of condensation into the liquid phase (Wu and Williams, 2010).

In addition to the solid carbon products that have been investigated in this work, the process of catalytic pyrolysis of waste plastics can also generate valuable gaseous. In particular, the production of hydrogen could contribute to the hydrogen economy, which plays an important role in the future energy system (Nnabuife et al., 2022). Yao et al. (Yao et al., 2018b) reported that the highest syngas production was obtained when polystyrene was converted in the presence of a sol–gel derived Ni/Al_2O_3 catalyst, which resulted in the generation of 62.26 mmol H_2 $g^{-1}_{plastic}$ and 36.10 mmol CO $g^{-1}_{plastic}$. Besides, the waxes produced from the high-density polyethylene pyrolysis process can be co-fed with vacuum gasoil for catalytic cracking, which exhibited a high yield of olefinic gaseous fraction and a naphtha with high content of *iso*-paraffin and olefins and low yield of aromatics (Rodriguez et al., 2020). Moreover, high-density polyethene pyrolysis waxes were reacted using fluidised catalytic cracking technology, and various products can be obtained, including dry gas, liquefied petroleum gas, naphtha, light cycle oil, heavy cycle oil, and coke (Rodriguez et al., 2019). Vela et al. (Vela et al., 2021) reported several hydrocracking techniques to improve waste plastic and vacuum gasoil blends, which revealed that the hydrocracking of blends (waste plastics/vacuum gasoil/plastic pyrolysis oil) resulted in naphtha and light cycle oil with reduced aromatic concentration, making them more appealing for inclusion in fuel pools within a refinery.

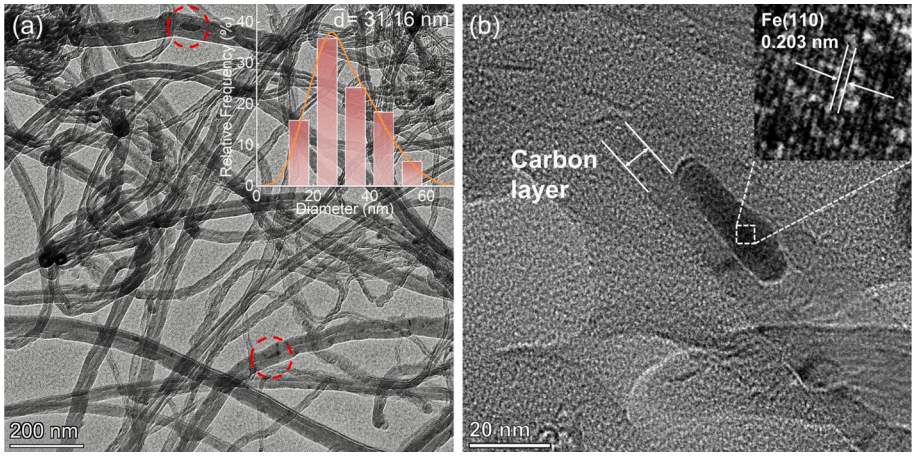

Fig. 5. TEM morphology analysis of PRWWP-2: (a) TEM image of CNTs and the outer diameters, (b) HRTEM image of CNTs.

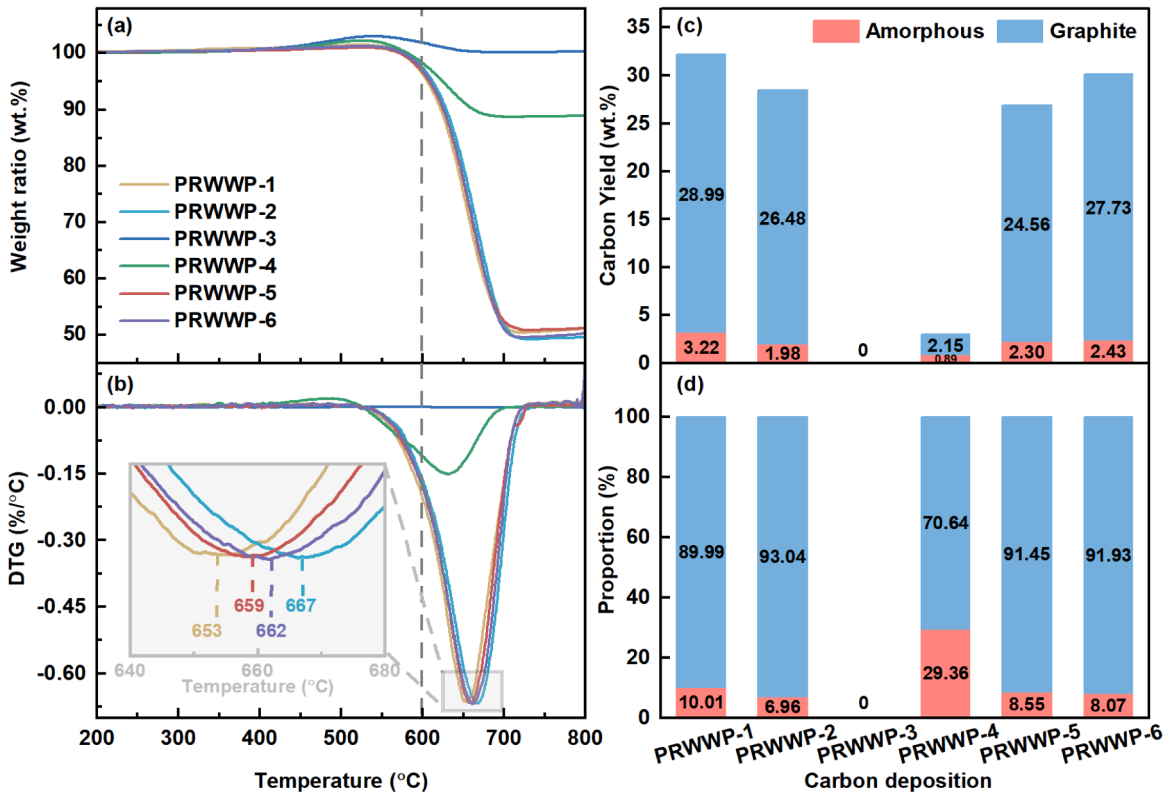

Fig. 6. (a) TGA-TPO patterns (b) DTG-TPO patterns (c) carbon yield (d) proportion of carbon types deposited on the reacted catalysts from RWWP.

4. Conclusion

In this work, the pyrolysis characteristic parameters of real-world waste plastics were determined, followed by a further study on high-value CNTs production by a catalytic-pyrolytic method. RWWP samples exhibited different pyrolysis behaviour. RWWP-1,2,5,6 were more feasible for generating volatile matter than RWWP-3,4. Besides, the results of the pyrolysis characteristic index showed that the efficiency of the pyrolysis process enhanced because of the increasing heating rate. This was reflected in the higher levels of pyrolysis intensity observed in the RWWP-1,2,5,6 samples. Furthermore, activation energy values from 131.04 kJ mol^{-1} to 171.04 kJ mol^{-1} of different RWWP were calculated by three methods (FWO, KAS, Starink methods), and the corresponding correlation coefficient (R^2) in the range of 90.67–99.99% suggested a reasonable result. Significantly, the Py-GC/MS experiments indicated that the possible compound for RWWP-1 was PS, RWWP-2 was PE, RWWP-3,4 was PET, and RWWP-5,6 was PP, respectively. The fresh catalyst and CNT products were then analyzed to validate the potential of producing high-value CNTs from the RWWP-1,2,5,6 samples. The carbon yield reached the top at 32.21 wt% in RWWP-1, and the highest CNTs purity of 93.04 % was obtained when RWWP-2 was performed as the feedstock. Overall, the results of this work serve to expand and deepen our understanding about the pyrolysis behavior of genuine waste plastics, and offer a sustainable solution to the worldwide waste plastic crisis by enabling the production of advanced carbon materials in an environmentally friendly manner.

Declaration of Competing Interest

The authors declare that they have no known competing financial interests or personal relationships that could have appeared to influence the work reported in this paper.

Data availability

The authors are unable or have chosen not to specify which data has been used.

Acknowledgment

The authors express their gratitude for the financial support received from the China Scholarship Council (reference number: 202009210017) and the European Union's Horizon 2020 research (Marie Skłodowska-Curie grant No 823745). They also acknowledge the financial backing from the National Natural Science Foundation of China (No 22111530110, 22106104) and the International Exchanges project through the Royal Society (IEC\NSFC\201146).

Appendix A. Supplementary material

Supplementary data to this article can be found online at https://doi.org/10.1016/j.wasman.2023.05.002.

References

Adyel, T.M., 2020. Accumulation of plastic waste during COVID-19. Science 369, 1314–1315. https://doi.org/10.1126/science.abd9925.

Akoueson, F., Chbib, C., Monchy, S., Paul-Pont, I., Doyen, P., Dehaut, A., Duflos, G., 2021. Identification and quantification of plastic additives using pyrolysis-GC/MS: A review. Sci. Total Environ. 773, 145073 https://doi.org/10.1016/j.scitotenv.2021.145073.

Alimi, O.S., Farner Budarz, J., Hernandez, L.M., Tufenkji, N., 2018. Microplastics and Nanoplastics in Aquatic Environments: Aggregation, Deposition, and Enhanced Contaminant Transport. Environ. Sci. Technol. 52, 1704–1724. https://doi.org/10.1021/acs.est.7b05559.

Al-Salem, S.M., Antelava, A., Constantinou, A., Manos, G., Dutta, A., 2017. A review on thermal and catalytic pyrolysis of plastic solid waste (PSW). J. Environ. Manage. 197, 177–198. https://doi.org/10.1016/j.jenvman.2017.03.084.

Amelinckx, S., Zhang, X.B., Bernaerts, D., Zhang, X.F., Ivanov, V., Nagy, J.B., 1994. A Formation Mechanism for Catalytically Grown Helix-Shaped Graphite Nanotubes. Science 265, 635–639. https://doi.org/10.1126/science.265.5172.635.

Cai, N., Xia, S., Zhang, X., Meng, Z., Bartocci, P., Fantozzi, F., Chen, Y., Chen, H., Williams, P.T., Yang, H., 2020. Preparation of Iron- and Nitrogen-Codoped Carbon Nanotubes from Waste Plastics Pyrolysis for the Oxygen Reduction Reaction. ChemSusChem 13, 938–944. https://doi.org/10.1002/cssc.201903293.

Cai, N., Li, X., Xia, S., Sun, L., Hu, J., Bartocci, P., Fantozzi, F., Williams, P.T., Yang, H., Chen, H., 2021a. Pyrolysis-catalysis of different waste plastics over Fe/Al2O3 catalyst: High-value hydrogen, liquid fuels, carbon nanotubes and possible reaction mechanisms. Energy Convers. Manage. 229, 113794 https://doi.org/10.1016/j.enconman.2020.113794.

Cai, N., Xia, S., Li, X., Sun, L., Bartocci, P., Fantozzi, F., Zhang, H., Chen, H., Williams, P. T., Yang, H., 2021b. Influence of the ratio of Fe/Al2O3 on waste polypropylene pyrolysis for high value-added products. J. Cleaner Prod. 315, 128240 https://doi.org/10.1016/j.jclepro.2021.128240.

Cao, B., Yuan, J.P., Jiang, D., Wang, S., Barati, B., Hu, Y.M., Yuan, C., Gong, X., Wang, Q., 2021. Seaweed-derived biochar with multiple active sites as a heterogeneous catalyst for converting macroalgae into acid-free biooil containing abundant ester and sugar substances. Fuel 285. https://doi.org/10.1016/j.fuel.2020.119164.

Chae, Y., An, Y.-J., 2018. Current research trends on plastic pollution and ecological impacts on the soil ecosystem: A review. Environ. Pollut. 240, 387–395. https://doi.org/10.1016/j.envpol.2018.05.008.

Chen, D., Christensen, K., Ochoafernandez, E., Yu, Z., Totdal, B., Latorre, N., Monzon, A., Holmen, A., 2005. Synthesis of carbon nanofibers: effects of Ni crystal size during methane decomposition. J. Catal. 229, 82–96. https://doi.org/10.1016/j.jcat.2004.10.017.

Chen, J.B., Mu, L., Jiang, B., Yin, H.C., Song, X.G., Li, A.M., 2015. TG/DSC-FTIR and Py-GC investigation on pyrolysis characteristics of petrochemical wastewater sludge. Bioresour. Technol. 192, 1–10. https://doi.org/10.1016/j.biortech.2015.05.031.

Chu, J.H., Liu, H.M., Salvo, A., 2021. Air pollution as a determinant of food delivery and related plastic waste. Nat. Hum. Behav. 5, 212. https://doi.org/10.1038/s41562-020-00961-1.

Dai, L.L., Zhou, N., Lv, Y.C., Cheng, Y.L., Wang, Y.P., Liu, Y.H., Cobb, K., Chen, P.L., Lei, H.W., Ruan, R.G., 2022. Pyrolysis technology for plastic waste recycling: A state-of-the-art review. Prog. Energy Combust. Sci. 93 https://doi.org/10.1016/j.pecs.2022.101021.

Das, P., Tiwari, P., 2017. Thermal degradation kinetics of plastics and model selection. Thermochim. Acta 654, 191–202. https://doi.org/10.1016/j.tca.2017.06.001.

Das, P., Tiwari, P., 2018. The effect of slow pyrolysis on the conversion of packaging waste plastics (PE and PP) into fuel. Waste Manage. (Oxford) 79, 615–624. https://doi.org/10.1016/j.wasman.2018.08.021.

Deck, C.P., Vecchio, K., 2006. Prediction of carbon nanotube growth success by the analysis of carbon–catalyst binary phase diagrams. Carbon 44, 267–275. https://doi.org/10.1016/j.carbon.2005.07.023.

Ding, Z.Y., Chen, H.S., Liu, J.Y., Cai, H.M., Evrendilek, F., Buyukada, M., 2021. Pyrolysis dynamics of two medical plastic wastes: Drivers, behaviors, evolved gases, reaction mechanisms, and pathways. J. Hazard. Mater. 402 https://doi.org/10.1016/j.jhazmat.2020.123472.

Ding, F., RoséN, A., Bolton, K., 2004. Molecular dynamics study of the catalyst particle size dependence on carbon nanotube growth. J. Chem. Phys. 121, 2775. https://doi.org/10.1063/1.1770424.

Fang, S.W., Yu, Z.S., Lin, Y.S., Hu, S.C., Liao, Y.F., Ma, X.Q., 2015. Thermogravimetric analysis of the co-pyrolysis of paper sludge and municipal solid waste. Energy Convers. Manage. 101, 626–631. https://doi.org/10.1016/j.enconman.2015.06.026.

Galgani, L., Loiselle, S.A., 2021. Plastic pollution impacts on marine carbon biogeochemistry. Environ. Pollut. 268, 115598 https://doi.org/10.1016/j.envpol.2020.115598.

Gao, N.B., Li, A.M., Quan, C., Du, L., Duan, Y., 2013. TG-FTIR and Py-GC/MS analysis on pyrolysis and combustion of pine sawdust. J. Anal. Appl. Pyrolysis 100, 26–32. https://doi.org/10.1016/j.jaap.2012.11.009.

Golunski, S., 2007. Why use platinum in catalytic converters. Platinum Met. Rev. 51, 162. https://doi.org/10.1595/147106707X205857.

He, M.Y., Sun, Y.H., Han, B.X., 2022. Green Carbon Science: Efficient Carbon Resource Processing, Utilization, and Recycling towards Carbon Neutrality. Angewandte Chemie-International Edition 61. https://doi.org/10.1002/anie.202112835.

Honus, S., Kumagai, S., Fedorko, G., Molnár, V., Yoshioka, T., 2018. Pyrolysis gases produced from individual and mixed PE, PP, PS, PVC, and PET—Part I: Production and physical properties. Fuel 221, 346–360. https://doi.org/10.1016/j.fuel.2018.02.074.

Igalavithana, A.D., Yuan, X., Attanayake, C.P., Wang, S., You, S., Tsang, D.C.W., Nzihou, A., Ok, Y.S., 2022. Sustainable management of plastic wastes in COVID-19 pandemic: The biochar solution. Environ. Res. 212 https://doi.org/10.1016/j.envres.2022.113495.

Jorio, A., Saito, R., 2021. Raman spectroscopy for carbon nanotube applications. J. Appl. Phys. 129, 021102 https://doi.org/10.1063/5.0030809.

Jung, S.H., Cho, M.H., Kang, B.S., Kim, J.S., 2010. Pyrolysis of a fraction of waste polypropylene and polyethylene for the recovery of BTX aromatics using a fluidized bed reactor. Fuel Process. Technol. 91, 277–284. https://doi.org/10.1016/j.fuproc.2009.10.009.

Kalantar-Zadeh, K., Tang, J.B., Daeneke, T., O'Mullane, A.P., Stewart, L.A., Liu, J., Majidi, C., Ruoff, R.S., Weiss, P.S., Dickey, M.D., 2019. Emergence of Liquid Metals in Nanotechnology. ACS Nano 13, 7388–7395. https://doi.org/10.1021/acsnano.9b04843.

Lebreton, L., Andrady, A., 2019. Future scenarios of global plastic waste generation and disposal. Palgrave Communications 5. https://doi.org/10.1057/s41599-018-0212-7.

Leslie, H.A., J. M. Van Velzen, M., Brandsma, S.H., Vethaak, D., Garcia-Vallejo, J.J., Lamoree, M.H., 2022. Discovery and quantification of plastic particle pollution in human blood. Environ. Int., 107199. https://doi.org/10.1016/j.envint.2022.107199.

Liu, Q.Y., Cai, N., Peng, B., Wu, C.F., Hong, R., Jiang, D.Y., Zhang, H.Y., 2022. Investigating the influences of metal-support interaction in Ni-Fe catalysts on the quality of carbon nanomaterials from waste polypropylene. Fuel Process. Technol. 236 https://doi.org/10.1016/j.fuproc.2022.107428.

Liu, Q., Wang, F., Hu, E., Hong, R., Li, T., Yuan, X., Cheng, X.-B., Cai, N., Xiao, R., Zhang, H., 2022. Nickel-iron nanoparticles encapsulated in carbon nanotubes prepared from waste plastics for low-temperature solid oxide fuel cells. iScience. https://doi.org/10.1016/j.isci.2022.104855.

Loy, A.C.M., Yusup, S., Chin, B.L.F., Gan, D.K.W., Shahbaz, M., Acda, M.N., Unrean, P., Rianawati, E., 2018. Comparative study of in-situ catalytic pyrolysis of rice husk for syngas production: Kinetics modelling and product gas analysis. J. Cleaner Prod. 197, 1231–1243. https://doi.org/10.1016/j.jclepro.2018.06.245.

Macleod, M., Arp, H.P.H., Tekman, M.B., Jahnke, A., 2021. The global threat from plastic pollution. Science 373, 61–65. https://doi.org/10.1126/science.abg5433.

Major, I., Pin, J.-M., Behazin, E., Rodriguez-Uribe, A., Misra, M., Mohanty, A., 2018. Graphitization of Miscanthus grass biocarbon enhanced by in situgenerated FeCo nanoparticles. Green Chem. 20, 2269–2278. https://doi.org/10.1039/c7gc03457a.

Maldonado-Hodar, F.J., Moreno-Castilla, C., Rivera-Utrilla, J., Hanzawa, Y., Yamada, Y., 2000. Catalytic graphitization of carbon aerogels by transition metals. Langmuir 16, 4367–4373. https://doi.org/10.1021/la991080r.

Martin, A.J., Mondelli, C., Jaydev, S.D., Perez-Ramirez, J., 2021. Catalytic processing of plastic waste on the rise. Chem 7, 1487–1533. https://doi.org/10.1016/j.chempr.2020.12.006.

Ming, X., Xu, F., Jiang, Y., Zong, P., Wang, B., Li, J., Qiao, Y., Tian, Y., 2020. Thermal degradation of food waste by TG-FTIR and Py-GC/MS: Pyrolysis behaviors, products, kinetic and thermodynamic analysis. J. Cleaner Prod. 244, 118713 https://doi.org/10.1016/j.jclepro.2019.118713.

Nnabuife, S.G., Ugbeh-Johnson, J., Okeke, N.E., Ogbonnaya, C., 2022. Present and Projected Developments in Hydrogen Production: A Technological Review. Carbon Capture Sci. Technol. 3, 100042 https://doi.org/10.1016/j.ccst.2022.100042.

Patnaik, S., Kumar, S., Panda, A.K., 2019. Kinetics of Thermal Degradation of Non-Woven Plastics: Model-Free Kinetic Approach. ChemistrySelect 4, 8054–8060. https://doi.org/10.1002/slct.201901114.

Peng, X.W., Ma, X.Q., Lin, Y.S., Guo, Z.G., Hu, S.C., Ning, X.X., Cao, Y.W., Zhang, Y.W., 2015. Co-pyrolysis between microalgae and textile dyeing sludge by TG-FTIR: Kinetics and products. Energy Convers. Manage. 100, 391–402. https://doi.org/10.1016/j.enconman.2015.05.025.

Qiao, Y., Xu, F., Xu, S., Yang, D., Wang, B., Ming, X., Hao, J., Tian, Y., 2018. Pyrolysis Characteristics and Kinetics of Typical Municipal Solid Waste Components and Their Mixture: Analytical TG-FTIR Study. Energy Fuel 32, 10801–10812. https://doi.org/10.1021/acs.energyfuels.8b02571.

Qu, Y., Li, A.M., Wang, D., Zhang, L., Ji, G.Z., 2019. Kinetic study of the effect of in-situ mineral solids on pyrolysis process of oil sludge. Chem. Eng. J. 374, 338–346. https://doi.org/10.1016/j.cej.2019.05.183.

Rodriguez, E., Gutierrez, A., Palos, R., Vela, F.J., Arandes, J.M., Bilbao, J., 2019. Fuel production by cracking of polyolefins pyrolysis waxes under fluid catalytic cracking (FCC) operating conditions. Waste Manage. (Oxford) 93, 162–172. https://doi.org/10.1016/j.wasman.2019.05.005.

Rodriguez, E., Palos, R., Gutierrez, A., Trueba, D., Arandes, J.M., Bilbao, J., 2020. Towards waste refinery: Co-feeding HDPE pyrolysis waxes with VGO into the catalytic cracking unit. Energy Convers. Manage. 207 https://doi.org/10.1016/j.enconman.2020.112554.

Sophonrat, N., Sandström, L., Johansson, A.-C., Yang, W., 2017. Co-pyrolysis of Mixed Plastics and Cellulose: An Interaction Study by Py-GC×GC/MS. Energy Fuel 31, 11078–11090. https://doi.org/10.1021/acs.energyfuels.7b01887.

Vela, F.J., Palos, R., Trueba, D., Bilbao, J., Arandes, J.M., Gutierrez, A., 2021. Different approaches to convert waste polyolefins into automotive fuels via hydrocracking with a NiW/HY catalyst. Fuel Process. Technol. 220 https://doi.org/10.1016/j.fuproc.2021.106891.

Wang, Y.Y., Bailey, J., Zhu, Y., Zhang, Y.R., Boetcher, S.K.S., Li, Y.L., Wu, C.F., 2022. Application of carbon nanotube prepared from waste plastic to phase change materials: The potential for battery thermal management. Waste Manage. (Oxford) 154, 96–104. https://doi.org/10.1016/j.wasman.2022.10.003.

Wang, J.Q., Shen, B.X., Lan, M.C., Kang, D.R., Wu, C.F., 2020. Carbon nanotubes (CNTs) production from catalytic pyrolysis of waste plastics: The influence of catalyst and reaction pressure. Catal. Today 351, 50–57. https://doi.org/10.1016/j.cattod.2019.01.058.

Weizhong, Q., Tang, L., Zhanwen, W., Fei, W., Zhifei, L., Guohua, L., Yongdan, L., 2004. Production of hydrogen and carbon nanotubes from methane decomposition in a two-stage fluidized bed reactor. "Appl. Catal. A" 260, 223–228. https://doi.org/10.1016/j.apcata.2003.10.018.

Williams, P.T., 2021. Hydrogen and Carbon Nanotubes from Pyrolysis-Catalysis of Waste Plastics: A Review. Waste Biomass Valorization 12, 1–28. https://doi.org/10.1007/s12649-020-01054-w.

Wu, C., Nahil, M.A., Miskolczi, N., Huang, J., Williams, P.T., 2014. Processing real-world waste plastics by pyrolysis-reforming for hydrogen and high-value carbon nanotubes. Environ. Sci. Technol. 48, 819–826. https://doi.org/10.1021/es402488b.

Wu, C.F., Williams, P.T., 2010. Pyrolysis-gasification of plastics, mixed plastics and real-world plastic waste with and without Ni-Mg-Al catalyst. Fuel 89, 3022–3032. https://doi.org/10.1016/j.fuel.2010.05.032.

Xia, W., Tang, J., Li, J.J., Zhang, S.H., Wu, K.C.W., He, J.P., Yamauchi, Y., 2019. Defect-Rich Graphene Nanomesh Produced by Thermal Exfoliation of Metal-Organic

Frameworks for the Oxygen Reduction Reaction. Angewandte Chemie-International Edition 58, 13354–13359. https://doi.org/10.1002/anie.201906870.

Xu, F.F., Wang, B., Yang, D., Hao, J.H., Qiao, Y.Y., Tian, Y.Y., 2018. Thermal degradation of typical plastics under high heating rate conditions by TG-FTIR: Pyrolysis behaviors and kinetic analysis. Energy Convers. Manage. 171, 1106–1115. https://doi.org/10.1016/j.enconman.2018.06.047.

Yan, N., 2022. Recycling plastic using a hybrid process. Science 378, 132–133. https://doi.org/10.1126/science.ade5658.

Yao, D., Zhang, Y., Williams, P.T., Yang, H., Chen, H., 2018a. Co-production of hydrogen and carbon nanotubes from real-world waste plastics: Influence of catalyst composition and operational parameters. "Appl. Catal. B" 221, 584–597. https://doi.org/10.1016/j.apcatb.2017.09.035.

Yao, D., Yang, H., Hu, Q., Chen, Y., Chen, H., Williams, P.T., 2021. Carbon nanotubes from post-consumer waste plastics: Investigations into catalyst metal and support material characteristics. "Appl. Catal. B" 280, 119413 https://doi.org/10.1016/j.apcatb.2020.119413.

Yao, D., Li, H., Mohan, B.C., Prabhakar, A.K., Dai, Y., Wang, C.-H., 2022. Conversion of Waste Plastic Packings to Carbon Nanomaterials: Investigation into Catalyst Material, Waste Type, and Product Applications. ACS Sustain. Chem. Eng. 10, 1125–1136. https://doi.org/10.1021/acssuschemeng.1c05945.

Yao, D.D., Yang, H.P., Chen, H.P., Williams, P.T., 2018b. Co-precipitation, impregnation and so-gel preparation of Ni catalysts for pyrolysis-catalytic steam reforming of waste plastics. Appl. Catal. B-Environm. 239, 565–577. https://doi.org/10.1016/j.apcatb.2018.07.075.

Yildiz, G., Ronsse, F., Venderbosch, R., Duren, R.V., Kersten, S.R.A., Prins, W., 2015. Effect of biomass ash in catalytic fast pyrolysis of pine wood. "Appl. Catal. B" 168–169, 203–211. https://doi.org/10.1016/j.apcatb.2014.12.044.

Zhang, Y., Fu, Z., Wang, W., Ji, G., Zhao, M., Li, A., 2022. Kinetics, Product Evolution, and Mechanism for the Pyrolysis of Typical Plastic Waste. ACS Sustain. Chem. Eng. 10, 91–103. https://doi.org/10.1021/acssuschemeng.1c04915.

Zou, H.H., Evrendilek, F., Liu, J.Y., Buyukada, M., 2019. Combustion behaviors of pileus and stipe parts of Lentinus edodes using thermogravimetric-mass spectrometry and Fourier transform infrared spectroscopy analyses: Thermal conversion, kinetic, thermodynamic, gas emission and optimization analyses. Bioresour. Technol. 288 https://doi.org/10.1016/j.biortech.2019.121481.